Porous Graphitic Carbon Nanosheets as a High-Rate Anode Material for Lithium-Ion Batteries

Long Chen,[†] Zhiyuan Wang,[†] Chunnian He,*[,†,‡] Naiqin Zhao,[†,‡] Chunsheng Shi,[†] Enzuo Liu,[†] and Jiajun Li[†]

[†]School of Materials Science and Engineering and Tianjin Key Laboratory of Composites and Functional Materials, Tianjin University, Tianjin 300072, China

[‡]Collaborative Innovation Center of Chemical Science and Engineering, Tianjin 300072, China

Ⓢ Supporting Information

ABSTRACT: Two-dimensional (2D) porous graphitic carbon nanosheets (PGC nanosheets) as a high-rate anode material for lithium storage were synthesized by an easy, low-cost, green, and scalable strategy that involves the preparation of the PGC nanosheets with Fe and Fe_3O_4 nanoparticles embedded (indicated with $(Fe\&Fe_3O_4)$@PGC nanosheets) using glucose as the carbon precursor, iron nitrate as the metal precursor, and a surface of sodium chloride as the template followed by the subsequent elimination of the Fe and Fe_3O_4 nanoparticles from the $(Fe\&Fe_3O_4)$@PGC nanosheets by acid dissolution. The unique 2D integrative features and porous graphitic characteristic of the carbon nanosheets with high porosity, high electronic conductivity, and outstanding mechanical flexibility and stability are very favorable for the fast and steady transfer of electrons and ions. As a consequence, a very high reversible capacity of up to 722 mAh/g at a current density of 100 mA/g after 100 cycles, a high rate capability (535, 380, 200, and 115 mAh/g at 1, 10, 20, and 30 C, respectively, 1 C = 372 mA/g), and a superior cycling performance at an ultrahigh rate (112 mAh/g at 30 C after 570 charge–discharge cycles) are achieved by using these nanosheets as a lithium-ion-battery anode material.

KEYWORDS: two dimensional, carbon nanosheets, high-rate anode, lithium-ion battery
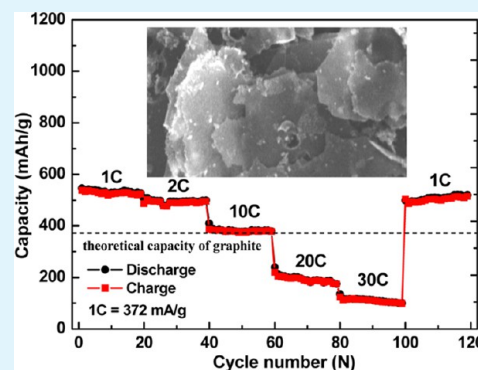
1. INTRODUCTION

Until now, graphite has always been the most commonly utilized commercial lithium-ion-battery (LIB) anode material because of its low cost, excellent cyclic stability, and low lithium intercalation potential regarding the lithium metal.[1−4] However, graphite's low theoretical capacity of 372 mAh/g and very limited rate performance by virtue of its low lithium diffusion coefficient cannot satisfy the urgent demand of promising power sources (such as electric vehicles (EVs) and hybrid electric vehicles (HEVs)) with high energy and power density. Moreover, the unwanted metallic lithium plating inevitably appears on the graphitic anode surface because of its working potential of around 0 V versus Li^+/Li, which would result in the damage of the solid electrolyte interface (SEI) film on the graphite surface, the decrease of cycling performance, and the raising of safety issues induced by the internal short-circuiting resulting from the formation of dendritic lithium.[5−7]

To circumvent the above issues, substantial research efforts have been devoted to employing novel carbon nanostructures with designed morphology, such as carbon nanotubes,[8] carbon nanofibers,[9,10] graphenes,[11−16] carbon nanobeads,[17] ordered mesoporous carbon,[18] hierarchically porous carbon,[19−22] hollow carbon nanospheres,[23−25] and their composites.[26−28] These nanostructures have multiple functionalities by engen-

dering additional sites for lithium-ion storage and thus they improve remarkably the lithium storage capacity. However, the high rate performance and cyclic stability at high rates of these materials, which are especially required for their applications in the HEVs and EVs, are still challenging.[8−25] As is known, the LIB rate performance, to a great extent, is decided by the transport speed of lithium ions and electrons within the electrolyte and the bulk electrode. Therefore, a favorable tactic for designing high-rate LIBs is to explore novel nanostructured materials that have high electronic conductivity for rapid electron transfer and well-built porous structures with large specific surface area and short diffusion distances for fast lithium-ion diffusion.[29−34]

In this work, we report a facile and scalable synthesis strategy to fabricate 2D porous graphitic carbon nanosheets (indicated as PGC nanosheets) with a thickness of about 50 nm for a high-rate LIB anode. In this methodology, the PGC nanosheets with Fe and Fe_3O_4 nanoparticles embedded (indicated with $(Fe\&Fe_3O_4)$@PGC nanosheets) were produced using glucose as the carbon precursor, iron nitrate as the metal precursor, and
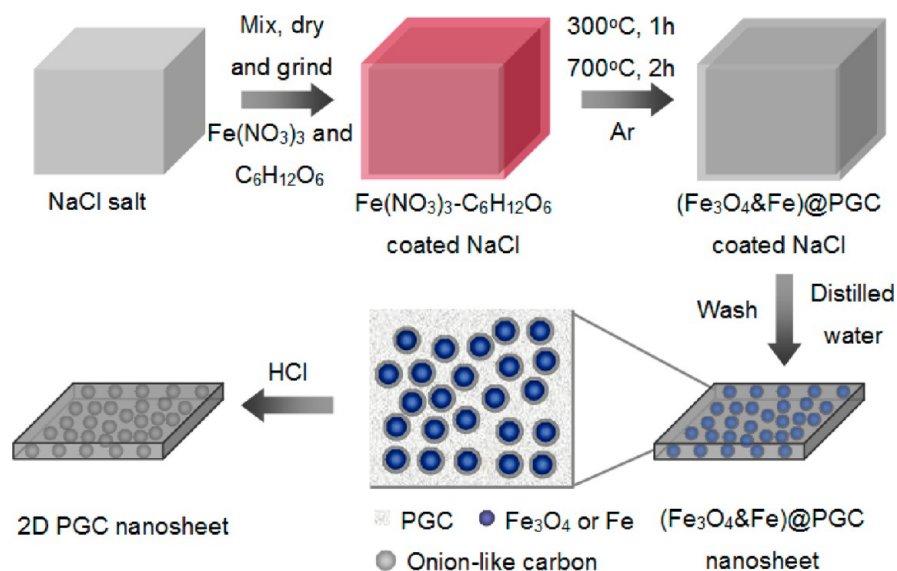
Figure 1. Illustration of the fabrication processes for 2D PGC nanosheets.

a surface of sodium chloride (NaCl) as the template. Next, the $(Fe\&Fe_3O_4)$@PGC nanosheets were immersed in acid to dissolve the Fe and Fe_3O_4 nanoparticles, and finally pure 2D PGC nanosheets were obtained. The unique 2D integrative feature and porous graphitic characteristic of the carbon nanosheets with high porosity, high electronic conductivity, and outstanding mechanical flexibility and stability are very favorable for the fast and steady transfer of electrons and ions, leading to a very high reversible capacity of up to 722 mAh/g at a current density of 100 mA/g after 100 cycles, a high rate capability (535, 380, 200, and 115 mAh/g at 1, 10, 20, and 30 C, respectively, 1 C = 372 mA/g), and a superior cycling performance at an ultrahigh rate (112 mAh/g at a high rate of 30 C after 570 cycles). Importantly, the approach for preparing such unique 2D porous graphitic nanostructures is easy, low-cost, environmentally friendly, and scalable and thus is very beneficial for the evolutive design of a LIB anode with improved high rate performance and cyclic stability performance at high rates.

2. EXPERIMENTAL SECTION

2.1. Synthesis of the 2D PGC Nanosheets. All chemicals, which were analytically pure and purchased from Tianjin Chemical Reagent Company, were used without further purification. To prepare 2D PGC nanosheets, 2.5 g of glucose, 1.68 g of $Fe(NO_3)_3 \cdot 9H_2O$, and 24.11 g of NaCl were dissolved in deionized water (75 mL) under intense stirring to obtain a homogeneous solution. The resulting solution was then placed in a vacuum furnace and maintained at 80 °C for 12 h to obtain solid materials. Subsequently, the solid materials were ground by agate mortar until a fine composite powder was obtained. For the carbonization, 4 g of the composite powder in a quartz boat was first heat-treated in a tubular furnace at 300 °C for 1 h and then at 700 °C for 2 h under Ar flow. After cooling to ambient temperature under Ar, the product was washed with deionized water several times to remove the NaCl, and a black powder (2D $(Fe\&Fe_3O_4)$@PGC nanosheets) was obtained. To obtain pure 2D PGC nanosheets, 100 mg of the black powder ($(Fe\&Fe_3O_4)$@PGC nanosheets) was immersed in 100 mL of a concentrated hydrochloric acid (HCl) solution (12 mol/L) and was then refluxed at 80 °C for 3 h with magnetic stirring to remove the Fe and Fe_3O_4 nanoparticles.

2.2. Characterization. The morphologies of the 2D $(Fe\&Fe_3O_4)$@PGC nanosheets and 2D PGC nanosheets were investigated by field-emission scanning electron microscopy (FE-SEM, JSM-6700F).

The microstructures of the $(Fe\&Fe_3O_4)$@PGC nanosheets and PGC nanosheets were analyzed using transmission electron microscope (TEM) and high-resolution TEM (HRTEM) performed on a FEI Tecnai G^2 F20 apparatus. X-ray diffraction (XRD) measurements were conducted by a Rigaku D/max diffractometer to ascertain the phases of the $(Fe\&Fe_3O_4)$@PGC and PGC nanosheets. A Raman spectrum of the PGC nanosheets was taken using a LabRAM HR Raman spectrometer. Nitrogen adsorption−desorption measurements were performed to determine the Brunauer−Emmett−Teller (BET) specific surface areas of PGC nanosheets using an autosorb iQ instrument (Quantachrome U.S.). The specific surface areas were calculated on the basis of the BET method, and the pore size distributions were obtained from the desorption branches of the isotherms according to the Barrett−Joyner−Halanda (BJH) model.

2.3. Electrochemical Measurements. A coin-type test cell (CR2032) was utilized to evaluate the electrochemical performance of the 2D PGC nanosheet electrode. The working electrode was produced by coating the mixture of active mass (2D PGC nanosheets), carbonaceous additive (acetylene black, 10 wt %), and poly(vinylidene difluoride) (PVDF, 10 wt %) binder on a copper foil, which was first dried in a vacuum furnace at 80 °C for 4 h and then at 120 °C for 12 h. The lithium metal was used as both the counter and reference electrode, and a Celgard 2400 polypropylene membrane was used as the separator. The electrolyte used in this work is a 1 M $LiPF_6$ solution in a mixture (1:1:1, in vol %) of dimethyl carbonate (DMC), ethylene carbonate (EC), and ethylmethyl carbonate (EMC). The cells were assembled in an argon-filled glovebox in which both the moisture and oxygen contents were controlled to be less than 0.1 ppm. Cyclic voltammetry (CV) was performed on a CHI660D electrochemical workstation at 0.1 mV/s in the 0.0−3.0 V voltage range. Galvanostatic charge−discharge cycles were tested by a LAND CT2001A electrochemical workstation at various current densities ranging from 100 to 11 160 mA/g between 3.00 and 0.005 V versus Li^+/Li at room temperature. All of the specific capacities in this work were estimated by using the weight of the active materials. Electrochemical impedance spectroscopy (EIS) experiments were carried out using a CHI660D electrochemical workstation. ac impedance measurements were conducted in the frequency range of 0.1−100 kHz at room temperature using an amplitude of 5 mV.

3. RESULTS AND DISCUSSION

3.1. Structural Characterizations of the 2D PGC Nanosheets. The overall synthesis for preparing 2D PGC nanosheets with a high graphitic degree and large surface area is schematically illustrated in Figure 1. In the synthesis of the 2D

PGC nanosheets, two strategies were adopted. First, the NaCl particle surface was utilized as the template for the 2D nanosheets. Second, glucose was chosen as the carbon precursor because it is environmentally friendly and easy to control.[35] During the synthesis, the carbon source (glucose), inorganic metal salts ($Fe(NO_3)_3$), and NaCl salt particles were first dissolved in distilled water to obtain a homogeneous solution. After heat-treating at 80 °C, the solution color changed from brown to yellow, the sample viscosity increased greatly, and then the polymerization of the glucose began, which resulted in the generation of a very thin frame homogeneously coated on the NaCl particle surface. Upon heating at high temperature under Ar, the carbonization of the glucose and decomposition of the inorganic metal salts took place, leading to the conversion of the thin frame to 2D magnetic PGC nanosheets ((Fe_3O_4&Fe)@PGC nanosheets). After removing NaCl with distilled water and magnetic nanoparticles (Fe_3O_4 and Fe) with HCl, the pure 2D PGC nanosheets with a high graphitic degree and large surface area were obtained. Generally, materials fabricated by liquid-phase synthesis methods[8,11,23−25] are dispersed in solvents, and tedious purification processes are thus required to obtain the pure materials, which would lead to agglomerations for the final solid materials obtained. The solid-phase carbonization method employed in this work provides an easy, green, and low-cost route to produce porous carbon materials directly on large scales (when we ran the reaction using 2.5 g of glucose precursor, ~0.72 g of the PGC nanosheets was obtained), which would be very beneficial for the wide application of these PGC nanosheets as a LIB anode material.

The phase structures of the as-prepared products ((Fe&Fe_3O_4)@PGC nanosheets) after water washing and the 2D PGC nanosheets obtained by removing magnetic nanoparticles from the (Fe&Fe_3O_4)@PGC nanosheets with HCl were detected by the wide-angle XRD that is displayed in Figure 2. As shown in the upper line of Figure 2a, the diffraction of the as-synthesized products exhibits a strong peak located at $2\theta = 26.2°$ and a series of peaks at 30−90°. The former peak is associated with the graphite (002) plane. For the latter peaks at 30−90°, the three sharp diffraction peaks at 44.6°, 65°, and 82.2° correspond to the reflections from the (100), (200), and (211) crystal planes of α-Fe (JCPDS 06-

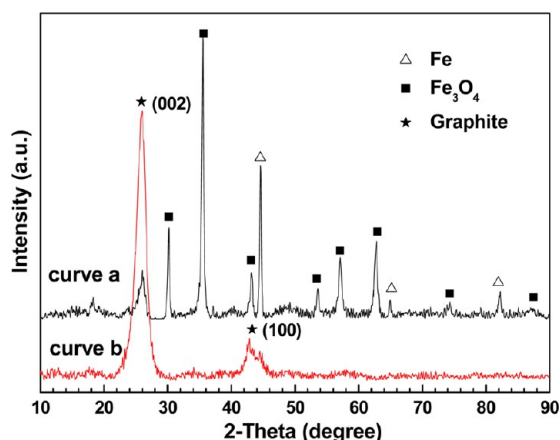0696), respectively, and the other peaks can be attributed to the Fe_3O_4 phase (JCPDS 19-0629). These results show that the iron species from $Fe(NO_3)_3 \cdot 9H_2O$ had been transformed into Fe or Fe_3O_4 during the carbonization process and that meanwhile graphitic carbon was also formed during the formation of Fe and Fe_3O_4. In addition, no NaCl phases were found in Figure 2a. This indicates that NaCl can be effectively removed from the (Fe&Fe_3O_4)@PGC nanosheets by the water-washing process. The bottom line of Figure 2b shows the XRD pattern of 2D PGC nanosheets obtained by removing magnetic nanoparticles from the (Fe&Fe_3O_4)@PGC nanosheets with HCl treatment. As can be seen, the peaks corresponding to Fe and Fe_3O_4 disappeared after the acid treatment, and the sharp two peaks were indexed to the graphitic carbon (002) and (100) planes, which indicate that the Fe and Fe_3O_4 can be easily leached out by HCl treatment and that pure PGC nanosheets have been synthesized. Moreover, the interplanar distance (d_{002}) of graphitic carbon in the nanosheets is about 0.342 nm calculated on the basis of the (002) peak in Figure 2b, which is very close to the ideal interplanar distance (0.335 nm) of graphite and thus validates that the PGC nanosheet sample has a well-developed graphitic structure.[36,37]

To confirm further the graphitic structure of the 2D PGC nanosheets, Raman spectroscopy was also carried out, and the result is shown in Figure 3a. As can be seen, the spectrum collected within the 800−2000 cm^{-1} range exhibits two evident peaks, corresponding to the D band (1342 cm^{-1}) and G band (1571 cm^{-1}), respectively. It is well-known that the D band arises from edges, defects, and disordered carbon, whereas the G band is ascribed to sp^2-hybridized carbon.[38,39] The integral intensity ratio of G peak to D peak (I_G/I_D) is usually used to evaluate the degree of crystallization of carbon materials. The value of I_G/I_D for the present 2D PGC nanosheets was calculated to be 1.32, further implying that the obtained nanosheets are mainly composed of well-crystallized graphitic carbon, in agreement with above XRD results.[38,39]

The morphology of the 2D PGC nanosheets was analyzed by SEM. Figure 3b,c shows the SEM images of the nanosheets. As can be seen, the sample consists of a mass of monodispersed and overlapped nanosheets with a thickness of about 50 nm and a lateral size of about 1−10 μm. This unique nanosheet material is very different from common porous carbon products generated from saccharide, which usually are carbon blocks with a size of several micrometers.[6,19−21,38] Therefore, this special 2D nanostructure is very helpful for the diffusion of electrolyte in the electrode because the thickness is reduced from micrometers to nanometers in 1D.[40,41] In addition, energy dispersive X-ray spectroscopy equipped with SEM was performed on the nanosheets (Figure S1), which further validates that Fe and Fe_3O_4 have been successfully removed from the PGC sample, in accordance with above XRD results. To elucidate the influence of NaCl on the 2D nanosheet formation, we have employed SEM analyses to investigate the carbonization products of the mixture ($Fe(NO_3)_3 \cdot 9H_2O$ and $C_6H_{12}O_6$) without adding the NaCl and the as-obtained carbonization products without eliminating the NaCl. According to Figure S2, the carbonization products produced without using NaCl contain only 3D carbon blocks with a size ranging from 1 to 100 μm, and no sheet-shaped nanostructures can be found in the products, which demonstrates that NaCl should have important influences on the formation of 2D PGC nanosheets.[40] When observing the SEM image (Figure S3) of
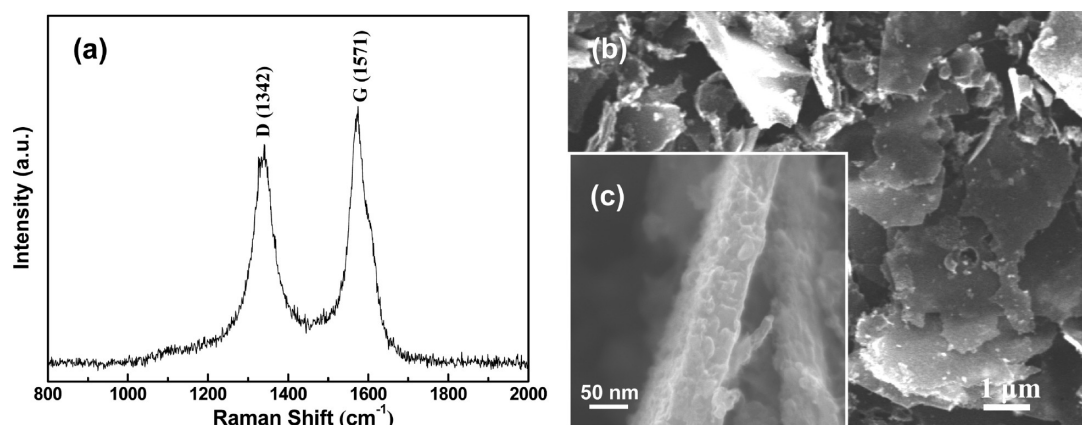

Figure 2. XRD patterns of the as-prepared products ((Fe&Fe_3O_4)@ PGC nanosheets) after water washing and the 2D PGC nanosheets obtained by removing magnetic nanoparticles from the (Fe&Fe_3O_4)@ PGC nanosheets with HCl treatment.

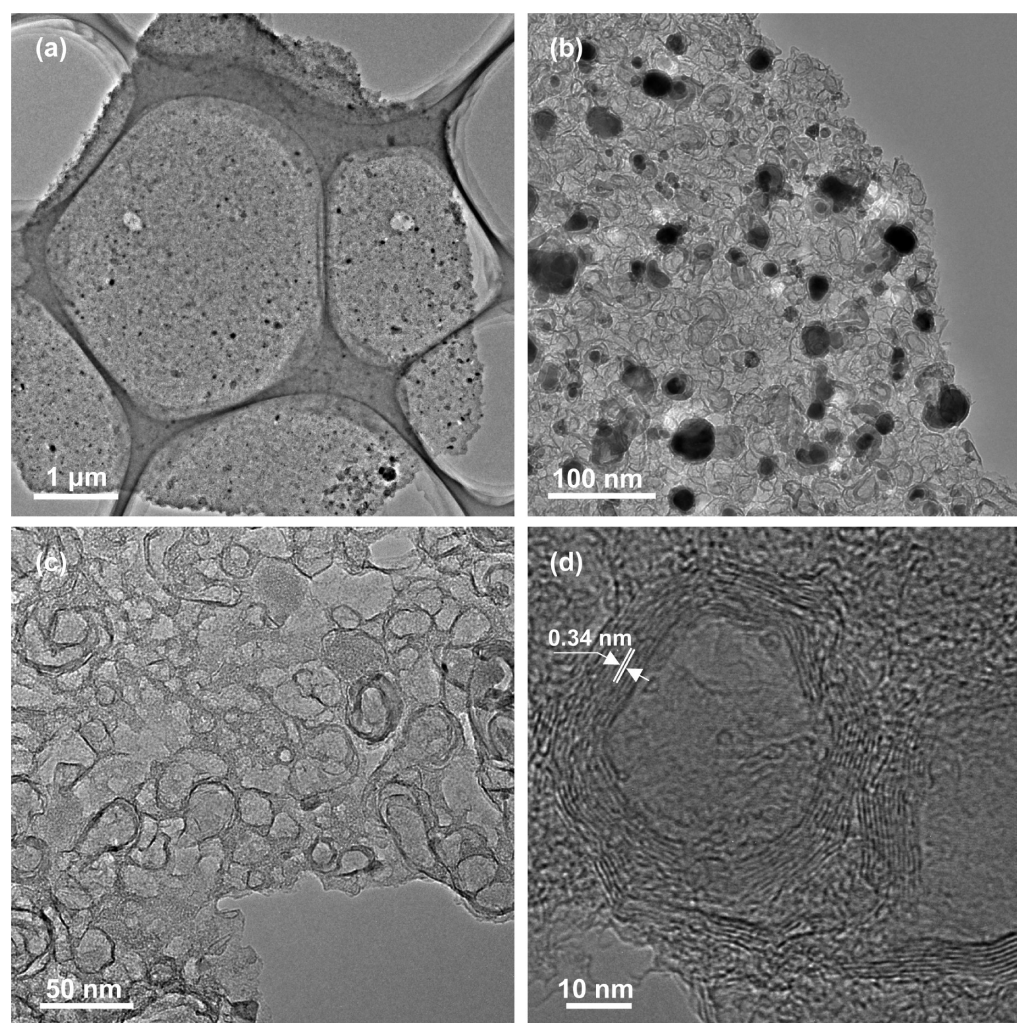**Figure 3.** (a) Raman spectrum and (b, c) SEM images of 2D PGC nanosheets.

Figure 4. TEM images of (a, b) 2D (Fe&Fe$_3$O$_4$)@PGC nanosheets and (c, d) 2D PGC nanosheets.

the as-obtained carbonization products without eliminating the NaCl, we can see that magnetic 2D PGC nanosheets were formed along with the surface of the NaCl particle (the locations of NaCl and magnetic PGC nanosheets were denoted in the SEM image of Figure S3), which suggests that the NaCl particle surface acts as the template for the formation of the 2D nanostructure.[40]

To obtain more detailed microstructural insight, the (Fe&Fe$_3$O$_4$)@PGC and PGC nanosheets were investigated by TEM and HRTEM observations (Figure 4). According to Figure 4a,b, we can see that after HCl treatment on the (Fe&Fe$_3$O$_4$)@PGC nanosheets, the Fe and Fe$_3$O$_4$ nanoparticles encapsulated in onionlike carbon layers have been completely removed, and a 2D porous graphitic structure consisting of well-developed interconnected mesopores and
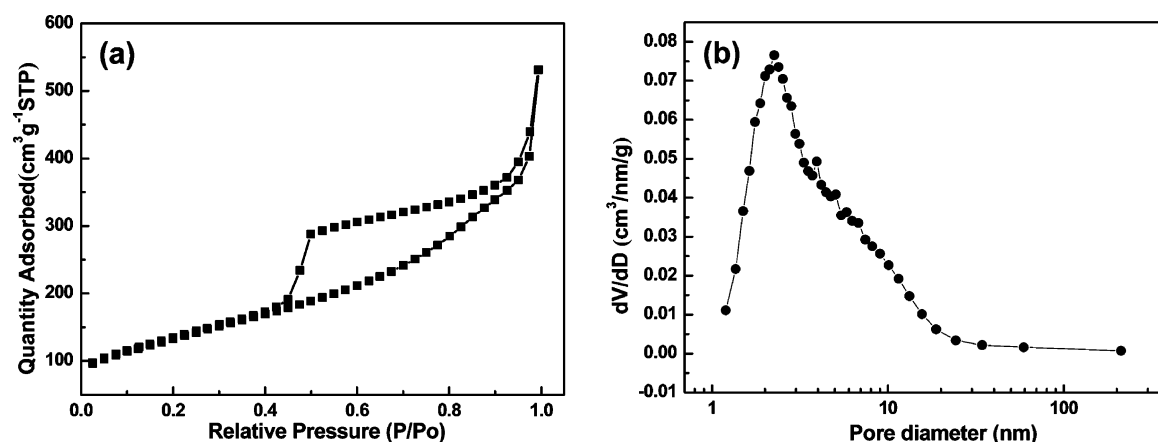
Figure 5. (a) Adsorption–desorption isotherms and (b) pore size distributions of 2D PGC nanosheets.

macropores was generated (Figure 4c,d). The walls of the porous structures were quite thin, with a thickness ranging from several nanometers to 10 nm. From a close look at the nanostructures by HRTEM (Figure 4d), it can be noticed that the walls of the pores were actually curved graphitic layers with a layer spacing of about 0.34 nm, which is very close to the typical value of graphite (0.335 nm) and is in good agreement with the above XRD and Raman results, suggesting that the stacking of graphene layers in the PGC nanosheets is very good. It has been reported that during the solid-phase catalytic process the graphitic carbon is mainly derived from the amorphous carbon that has tight contact with the catalyst nanoparticles;[42] therefore, all graphitic layers in the nanosheets present circlelike structures with various curvature.

Figure 5 shows the N_2 adsorption–desorption isotherms and pore size distributions of the 2D PGC nanosheets. As shown in Figure 5a, the N_2 adsorption–desorption isotherms of the nanosheets are typical of type IV according to the International Union of Pure and Applied Chemistry nomenclature, and they exhibit a prominent hysteresis loop at a relative pressure in the range of 0.45–0.97, which suggests a mesoporous structure as well as a narrow mesopore size distribution for the PGC nanosheets. In addition, a steep increase of N_2 uptake above 0.97 and a slow increase of N_2 uptake below 0.45 can also be observed, indicating that the nanosheets should also have macropores and micropores in their pore structure. On the basis of the above results, we can speculate that the pore structure of 2D PGC nanosheets is hierarchical because of the simultaneous presence of macropores, mesopores, and micropores, which can be further verified by the pore size distribution plot of Figure 5b. From the pore size distribution maximum in Figure 5b, the pore size was estimated to be about 2.26 nm, and the 2D PGC nanosheets show a BET specific surface area of ~469.48 m^2/g and a pore volume of ~0.83 cm^3/g. These evidences revealed that after the metal-catalyst-assisted pyrolysis and carbonization, highly porous graphitic carbon was synthesized. The pores in the PGC nanosheets were probably induced by the catalyzation effect and/or the elimination of the Fe or Fe_3O_4 nanoparticles from the nanosheets. In addition, the rapid gas emission during the high-temperature pyrolysis may produce new pores/voids, which have been confirmed in the above HRTEM results. Overall, the above XRD, TEM, and BET results demonstrate that the 2D PGC nanosheets with well-graphitized structure and high electronic conductivity may be very favorable to the

fast transfer of electrons and that the well-developed 2D porous structures with a large specific surface area may be very beneficial for the rapid diffusion of electrolyte ions, which suggests that these 2D PGC nanosheets can act as a superior anode material for LIBs.[27,38]

3.2. Electrochemical Properties of the 2D PGC Nanosheet Electrode. The lithium-ion insertion/extraction reactions of the 2D PGC nanosheet electrode were first investigated by CV experiments. Figure 6 shows representative
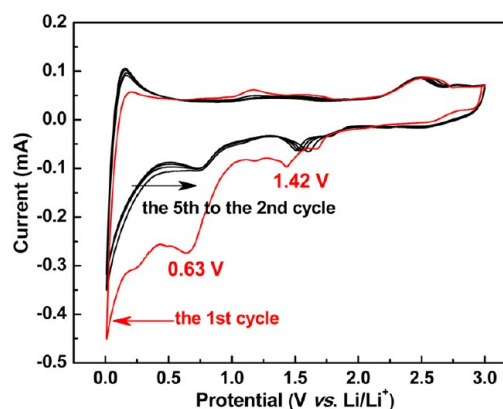

Figure 6. Representative CV curves of PGC nanosheet electrode.

CV curves of the nanosheet electrode conducted over voltages between 3.0 and 0.0 V at a scanning rate of 0.5 mV/s. In the first scanning cycle, we can clearly see two obvious cathodic current peaks located at around 0.63 and 1.42 V, although they disappeared during the second cycle. This result may be attributed to some irreversible reactions associated with the decomposition of electrolyte, the formation of a SEI film, and/ or the loss of some irreversible lithium storage sites during the initial cathodic scan.[10−15] In addition, it should be noted that after the initial scanning cycle the CV profiles almost overlapped, which indicates that the structural integrity of the nanosheet electrode is well preserved during subsequent charge−discharge cycles.[40] Moreover, the typical CV characteristics of PGC nanosheets are completely different from those of reduction/oxidation reactions of Fe/Fe_3O_4,[43−45] further indicating that the Fe/Fe_3O_4 nanoparticles have been completely removed from the nanosheets or that the very few residual Fe/Fe_3O_4 nanoparticles in the PGC nanosheets do
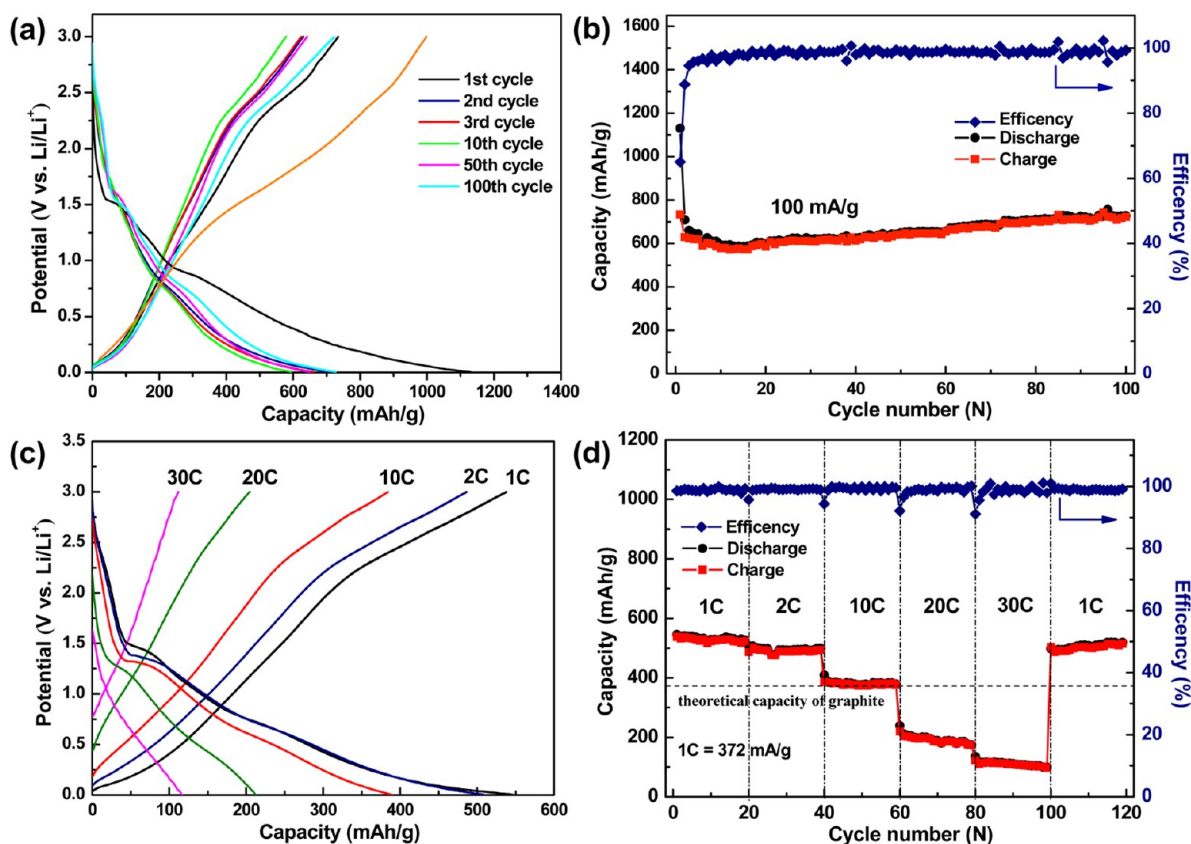
Figure 7. (a) Galvanostatic charge−discharge profile and (b) cycle performance and Coulombic efficiency of the PGC nanosheet electrode at a low current rate of 100 mA/g. (c) Galvanostatic charge−discharge profiles of PGC nanosheets at different C rates. (d) Rate capabilities and cycle performance of PGC nanosheet electrodes cycled at different current rates from 1 to 30 C (1 C = 372 mA/g).

not have any significant effect on the specific capacity of the electrode.

Figure 7a depicts the galvanostatic charge−discharge profiles of the 2D PGC nanosheet electrode at 100 mA/g within a cutoff voltage window of 0.005−3.0 V versus Li$^+$/Li. As can be seen, the charge and discharge curves exhibit a common shape that is similar to other carbonaceous nanostructures.[22−25] In the initial discharge curve, the voltage drops fast, with two plateaus appearing at around 1.5 and 0.9 V and most of the discharge capacity decreasing between 0.005 and 0.9 V. As for the charge curves, we can observe that the reversible capacity increases rapidly at the voltage range of 0.02−3 V and thus the charge curves are nearly steep lines at 0.02−3 V. In addition, it is worth noting that the two plateaus located at around 1.5 and 0.9 V in the first discharge process disappeared after the first cycle, which may be due to the irreversible insertion of lithium into the deep-seated superfine micropores.[22−25]

The cycling performance of the 2D PGC nanosheet electrode, measured at 100 mA/g for 100 cycles, is displayed in Figure 7b. As can be seen, the first discharge and charge capacities were 1130 and 734 mAh/g, respectively, leading to a Coulombic efficiency of ∼65%. The relatively low Coulombic efficiency during the initial cycle is mainly attributed to the irreversible capacity loss, which is induced by the decomposition of electrolyte and the formation of the SEI film. However, the Coulombic efficiency increases rapidly to 89% in the second cycle and 99% in the third cycle and then is maintained as high as 100% afterwards. After 100 cycles, the reversible capacity of the 2D PGC nanosheets was maintained at 722 mAh/g, which is 98% of the initial reversible capacity

and is remarkably larger than that of the theoretical capacity of graphite (∼372 mAh/g). This evidence indicates that our nanosheet electrode possesses superior lithium storage capability and outstanding cycling stability.[40] To investigate further the effect of the 2D structure on the electrochemical performance, the cycling performance of the 3D carbon block synthesized without NaCl was also studied, and the result is shown in Figure S4. As can be seen, the carbon block shows a much lower Coulombic efficiency of about 31% in the initial cycle and a reversible capacity of about 210 mAh/g than that of 2D PGC nanosheets, which indicates that the much shorter lithium-ion diffusion path of the 2D nanosheet structure compared to that of the 3D carbon block is very favorable for the fast and effective lithium-ion insertion/extraction and thus results in a much higher reversible capacity than that for the 3D carbon block.[40,46,47]

Figure 7c,d shows the rate performance of the PGC nanosheet electrodes at different high current rates (from 1 to 30 C, 1 C = 372 mA/g). At a charge−discharge rate of 1 C, a reversible capacity of 535 mAh/g was obtained, indicating a high reversible capacity of the PGC nanosheet electrodes.[43] When the current rate is increased to high rates of 2 and 10 C, the electrode still can deliver 500 and 380 mAh/g, respectively, which is larger than the theoretical capacity of a commercial graphite anode (∼372 mAh/g).[43] Even at ultrahigh current rates of 20 and 30 C, large reversible capacities of 200 and 115 mAh/g are still obtained, respectively. Remarkably, when the current rate was restored to 1 C after 100 cycles at different rates, a reversible capacity was still retained at 520 mAh/g after 120 cycles. Moreover, the kinetics features of the charge−
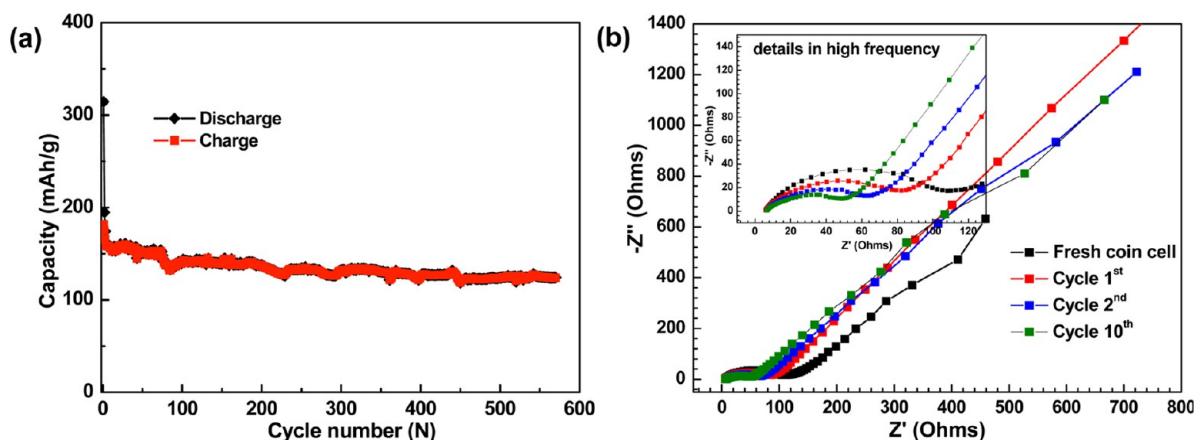
Figure 8. (a) Cycle performance of the PGC nanosheet electrode at a very high rate of 30 C between 3.0 and 0.005 V vs Li$^+$/Li. (b) Nyquist plots of the 2D PGC nanosheet electrode of the pristine cell and the first, second, and 10th charge−discharge cycles, with an amplitude of 5.0 mV in the frequency range from 100 kHz to 10 mHz. The inset in panel b shows the amplified spectra at the high-frequency region.
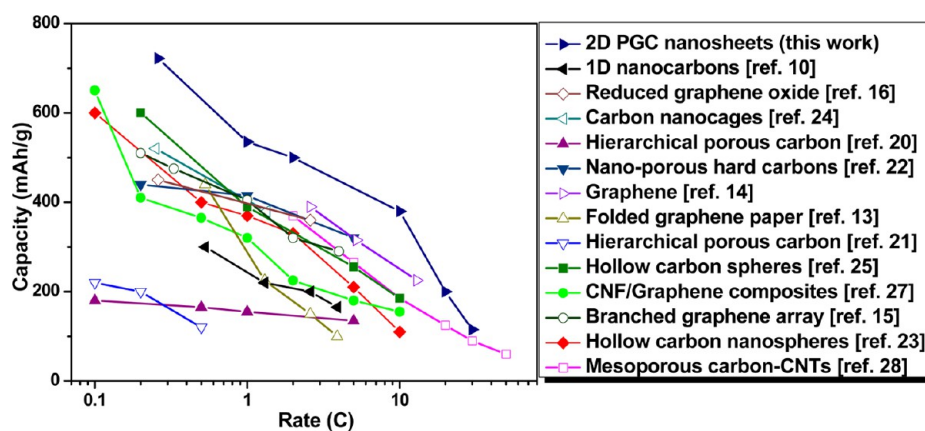

Figure 9. Comparison of reversible capacity at different current rates between the 2D PGC nanosheets and the carbon-based anodes previously reported.

discharge curves at high rates is still preserved similar to that at low rates (Figure 7c).[43] These results suggest that the 2D PGC nanosheets possess an easy charge-transport process and that the structure of the nanosheets remains extraordinarily stable even under high rate cycling. To confirm further the excellent cycling performance at a higher rate of 30 C, the cyclability of the present 2D PGC nanosheet electrode has been studied upon 570 cycles, and the result is exhibited in Figure 8a. As can be seen, the reversible capacity at a 30 C rate is 170 mAh/g in the initial cycle, 132 mAh/g in the 300th cycle, and 112 mAh/g in the 570th cycle, which further indicates that this interesting nanosheet electrode has superior cycling stability even at very high charge−discharge rates.[46,47]

To understand the reasons for the excellent rate performance of the 2D PGC nanosheet, EIS measurements were performed, and the results are displayed in Figure 8b. As can be seen, the impedance spectra obtained at different cycles (pristine electrode, first cycle, second cycles, and 10th cycles) are composed of a depressed semicircle arc in the high-to-medium frequency region and a linear tail in the low-frequency region. The semicircle at high frequency is an indication of SEI resistance (R_{SEI}) and contact resistance (R_f), the semicircle across the medium-frequency region represents the charge-transfer impedance (R_{ct}) between the electrode and the electrolyte, and the linear tail is the Warburg impedance (Z_w) associated with the diffusion of lithium ions in the carbon electrodes (R_e).[17,40,47] According to Figure 8b, we find that the diameters of the semicircles at both the high and medium frequencies decrease obviously with the increasing cycle numbers from the pristine coin cell to the 10th cycle, indicating depressed R_f and R_{ct} resistances. This result implies that the nanosheet electrode possesses a high electronic conductivity and a low contact and charge-transfer resistances, which are very beneficial for the fast insertion/extraction of lithium ions and thus results in a remarkable improvement of the rate performance of the nanosheet electrode.[17,40,46,47]

A comparison of traditional mesoporous carbon, hierarchical porous carbon, carbon nanosperes, graphene, carbon nanotubes, and their composites[11,14,16,17,20−28] with our 2D PGC nanosheets demonstrates a much larger reversible capacity and superior cycling performance at high charge−discharge rates (Figure 9). The outstanding electrochemical performance of these 2D nanosheets is due to the ultrathin, well-graphitized sheet-shaped 2D nanostructures as well as the large specific surface area and the porous structures.[40,46,47] First, the 2D integrative feature and porous nature of the nanosheets can ensure a large contact area between the electrode and electrolyte, which is very beneficial for the access of liquid electrolyte into the interior of the bulk electrode as well as the rapid and efficient transport of lithium ions into the deep locations of the stacked graphene layers.[28,40,46−49] Furthermore, the 2D ultrathin structure of our nanosheets is also very

favorable for the adsorption of lithium ions on both sides, edges, and other defects of these nanosheets and thus leads to high lithium storage capability.[13−15,40,46,47] Second, the well-graphitized micrometer-sized carbon nanosheets can form a continuous conductive network, which gives rise to the very high electronic conductivity of the overall electrode and is thus very beneficial for improving the rate performance of the electrode.[40,49] Third, the nanosheets with outstanding mechanical flexibility and stability can accommodate the volume changes upon lithium insertion and thus can preserve the structural integrity of the whole electrode.[40,46,49] Finally, the abundant macropores and mesopores can alleviate the local volume expansions of the nanosheet electrode during the charge−discharge processes, which can endow the electrode with structural integrity and stability and thus lead to superior lithium storage capacity and cycling stability at high rates.[28,40,46,50]

4. CONCLUSIONS

Two-dimensional PGC nanosheets with a thickness of about 50 nm for generating a high-rate LIB anode were synthesized by an easy, low-cost, green, and scalable method. In this strategy, the 2D PGC nanosheets with Fe and Fe_3O_4 nanoparticles embedded ((Fe&Fe_3O_4)@PGC nanosheets) were first fabricated using glucose as the carbon precursor, iron nitrate as the metal precursor, and a surface of sodium chloride as the template. Next, the (Fe&Fe_3O_4)@PGC nanosheets were immersed in acid to dissolve the Fe and Fe_3O_4 nanoparticles to obtain pure 2D PGC nanosheets. Such unique 2D features and the porous graphitic nature of the carbon nanosheets with high porosity, high electronic conductivity, and outstanding mechanical flexibility and stability are very favorable to the fast and steady transfer of electrons and ions, thereby leading to a very high reversible capacity of up to 722 mAh/g at a current density of 100 mA/g after 100 cycles, a high rate capability (535, 380, 200, and 115 mAh/g at 1, 10, 20, and 30 C, respectively, 1 C = 372 mA/g), and a superior cycling performance at very high rate (112 mAh/g at a high rate of 30 C after 570 cycles). Moreover, these synthetic procedures can be extended to various 2D inorganic-nanoparticle/carbon hybrid nanosheets, which may potentially be applied to electrodes, catalysts, sensors, adsorbents, and so on.

■ ASSOCIATED CONTENT

Ⓢ Supporting Information
EDX spectrum of a typical PGC nanosheet, SEM images of the carbonization products synthesized without NaCl and the carbonization products before eliminating the NaCl, and the cycle performance and Coulombic efficiency of the 3D carbon block produced without NaCl. This material is available free of charge via the Internet at http://pubs.acs.org.

■ AUTHOR INFORMATION

Corresponding Author
*E-mail: cnhe08@tju.edu.cn.

Notes
The authors declare no competing financial interest.

■ ACKNOWLEDGMENTS

■ REFERENCES

(1) Kang, B.; Ceder, G. Nature 2009, 458, 190−193.
(2) Tarascon, J. M.; Armand, M. Nature 2001, 414, 359−367.
(3) Simon, P.; Gogotsi, Y. Nat. Mater. 2008, 7, 845−854.
(4) Tang, K.; White, R. J.; Mu, X.; Titirici, M. M.; van Aken, P. A.; Maier, J. ChemSusChem 2012, 5, 400−403.
(5) Dahn, J. R.; Zheng, T.; Liu, Y.; Xue, J. S. Science 1995, 270, 590−593.
(6) Kaskhedikar, N. A.; Maier, J. Adv. Mater. 2009, 21, 2664−2680.
(7) Wang, H. Y.; Abe, T.; Maruyama, S.; Iriyama, Y.; Ogumi, Z.; Yoshikawa, K. Adv. Mater. 2005, 17, 2857−2860.
(8) Wang, X. X.; Wang, J. N.; Chang, H.; Zhang, Y. F. Adv. Funct. Mater. 2007, 17, 3613−3618.
(9) Maruyama, S. H.; Zhuang, G. Z.; Wang, H. Y.; Fukutsuka, T.; Miyazaki, K.; Abe, T. Carbon 2013, 57, 539−540.
(10) Sun, Q.; Zhang, X. Q.; Han, F.; Li, W. C.; Lu, A. H. J. Mater. Chem. 2012, 22, 17049−17054.
(11) Yoo, E. J.; Kim, J.; Hosono, E.; Zhou, H. S.; Kudo, T.; Honma, I. Nano Lett. 2008, 8, 2277−2282.
(12) Wang, G.; Shen, X.; Yao, J.; Park, J. Carbon 2009, 47, 2049−2053.
(13) Liu, F.; Song, S. Y.; Xue, D. F.; Zhang, H. J. Adv. Mater. 2012, 24, 1089−1094.
(14) Chen, X. C.; Wei, W.; Lv, W.; Su, F. Y.; He, Y. B.; Li, B. H. Chem. Commun. 2012, 48, 5904−5906.
(15) Kim, H. J.; Wen, Z. H.; Yu., K.; Mao, O.; Chen, J. H. J. Mater. Chem. 2012, 22, 15514−15518.
(16) Wan, D. Y.; Yang, C. Y.; Lin, T. Q.; Tang, Y. F.; Zhou, M.; Zhong, Y. J. ACS Nano 2012, 6, 9068−9078.
(17) Chen, S. Q.; Yeoh, W. K.; Liu, Q.; Wang, G. X. Carbon 2012, 50, 4557−4565.
(18) Zhou, H. S.; Zhu, S. M.; Hibino, M.; Honma, I.; Ichihara, M. Adv. Mater. 2003, 15, 2107−2111.
(19) Hu, Y. S.; Adelhelm, P.; Smarsly, B. M.; Hore, S.; Antonietti, M.; Maier, J. Adv. Funct. Mater. 2007, 17, 1873−1878.
(20) Yang, J.; Zhou, X. Y.; Zou, Y. L.; Tang, J. J. Electrochim. Acta 2011, 56, 8576−8581.
(21) Yia, J.; Li, X. P.; Hu, S. J.; Li, W. S.; Zhou, L.; Xu, M. Q. J. Power Sources 2011, 196, 6670−6675.
(22) Yang, J.; Zhou, X. Y.; Li, J.; Zou, Y. L.; Tang, J. J. Mater. Chem. Phys. 2012, 135, 445−450.
(23) Han, F. D.; Bai, Y. J.; Liu, R.; Yao, B.; Qi, Y. X.; Lun, N. Adv. Energy Mater. 2011, 1, 798−801.
(24) Li, G. D.; Xu, L. Q.; Hao, Q.; Wang, M.; Qian, Y. T. RSC Adv. 2012, 2, 284−291.
(25) Yang, S. B.; Feng, X. L.; Zhi, L. J.; Cao, Q.; Maier, J.; Mullen, K. Adv. Mater. 2010, 22, 838−842.
(26) Zhang, J.; Hu, Y. S.; Tessonnier, J. P.; Weinberg, G.; Maier, J.; Schlogl, R. Adv. Mater. 2008, 20, 1450−1455.
(27) Fan, Z. J.; Yan, J.; Wei, T.; Ning, G. Q.; Zhi, L. J.; Liu, J. C. ACS Nano 2011, 5, 2787−2794.
(28) Guo, B.; Wang, X.; Fulvio, P. F.; Chi, M.; Mahurin, S. M.; Sun, X. G. Adv. Mater. 2011, 23, 4661−4666.
(29) Mukherjee, R.; Krishnan, R.; Lu, T. M.; Koratkar, N. Nano Energy 2012, 1, 518−533.
(30) Kang, B.; Ceder, G. Nature 2009, 458, 190−193.
(31) Herle, P. S.; Ellis, B.; Coombs, N.; Nazar, L. F. Nat. Mater. 2004, 3, 147−152.

9544

dx.doi.org/10.1021/am402368p | ACS Appl. Mater. Interfaces 2013, 5, 9537−9545

(32) Chan, K. C.; Zhang, X. F.; Cui, Y. *Nano Lett.* **2008**, *8*, 307−309.

(33) Krishnan, R.; Lu, T. M.; Koratkar, N. *Nano Lett.* **2011**, *11*, 377−384.

(34) Ghosh, P.; Mahanty, S.; Basu, R. N. *Electrochim. Acta* **2009**, *54*, 1654−1661.

(35) Sun, X. M.; Li, Y. D. *Angew. Chem., Int. Ed.* **2004**, *43*, 597−601.

(36) Huang, W. T.; Zhang, H.; Huang, Y. Q.; Wang, W. K.; Wei, S. C. *Carbon* **2011**, *49*, 838−843.

(37) Hu, J.; Wang, H. L.; Gao, Q. M.; Guo, H. L. *Carbon* **2010**, *48*, 3599−3606.

(38) Wang, D. W.; Li, F.; Liu, M.; Lu, G. Q.; Cheng, H. M. *Angew. Chem., Int. Ed.* **2008**, *47*, 373−376.

(39) Huang, C. H.; Doong, R. A.; Gu, D.; Zhao, D. Y. *Carbon* **2011**, *49*, 3055−3064.

(40) He, C. N.; Wu, S.; Zhao, N. Q.; Shi, C. S.; Liu, E. Z.; Li, J. J. *ACS Nano* **2013**, *7*, 4459−4469.

(41) Zhao, N. Q.; Wu, S.; He, C. N.; Shi, C. S.; Liu, E. Z.; Du, X. X.; Li, J. J. *Mater. Lett.* **2012**, *87*, 77−79.

(42) Wang, Z. L.; Zhang, X. B.; Liu, X. J.; Lv, M. F.; Yang, K. Y.; Meng, J. *Carbon* **2011**, *49*, 161−169.

(43) Jia, X. L.; Chen, Z.; Cui, X.; Peng, Y. T.; Wang, X. L.; Wang, G. *ACS Nano* **2012**, *6*, 9911−9919.

(44) Su, Y. Z.; Li, S.; Wu, D. Q.; Zhang, F.; Liang, H. W.; Gao, P. F. *ACS Nano* **2012**, *6*, 8349−8356.

(45) Jang, B.; Park, M.; Chae, O. B.; Park, S. J.; Kim, Y. J.; Seung, M. O. *J. Am. Chem. Soc.* **2012**, *134*, 15010−15015.

(46) Fang, Y.; Lv, Y. Y.; Che, R. C.; Wu, H. Y.; Zhang, X. H.; Gu, D.; Zheng, G. F.; Zhao, D. Y. *J. Am. Chem. Soc.* **2013**, *135*, 1524−1530.

(47) Yin, S. Y.; Zhang, Y. Y.; Kong, J. H.; Zou, C. J.; Li, C. M.; Lu, X. H.; Ma, J.; Boey, F. Y. C.; Chen, X. D. *ACS Nano* **2011**, *5*, 3831−3838.

(48) Han, F. D.; Bai, Y. J.; Liu, R.; Yao, B.; Qi, Y. X.; Lun, N.; Zhang, J. X. *Adv. Energy Mater.* **2011**, *1*, 798−801.

(49) Wang, B.; Li, X. L.; Zhang, X. F.; Luo, B.; Jin, M. H.; Liang, M. H.; Dayeh, S. A.; Picraux, S. T.; Zhi, L. J. *ACS Nano* **2013**, *7*, 1437−1445.

(50) Zhao, N. Q.; Wu, S.; He, C. N.; Shi, C. S.; Liu, E. Z.; Du, X. X.; Li, J. J. *Carbon* **2013**, *57*, 130−138.